

ChimeraLM detects amplification artifacts for
accurate structural variant calling in long-read
single-cell sequencing

Yangyang Li^{1†}, Qingxiang Guo^{1†}, Rendong Yang^{1,2*}

¹Department of Urology, Northwestern University Feinberg School of Medicine, 303 E Superior St, Chicago, 60611, IL, USA.

²Robert H. Lurie Comprehensive Cancer Center, Northwestern University Feinberg School of Medicine, 675 N St Clair St, Chicago, 60611, IL, USA.

*Corresponding author(s). E-mail(s): rendong.yang@northwestern.edu;
Contributing authors: yangyang.li@northwestern.edu;

qingxiang.guo@northwestern.edu;

†These authors contributed equally to this work.

Abstract

Single-cell genomics enables unprecedented cellular heterogeneity insights but faces a fundamental challenge: Whole Genome Amplification (WGA) introduces chimeric artifacts that generate false Structural Variations (SVs), undermining biological interpretations. Current computational methods cannot distinguish amplification-induced artifacts from genuine rearrangements. Here we present ChimeraLM, a genomic language model that learns sequence-level features discriminating biological sequences from WGA artifacts. Validated on nanopore data, ChimeraLM achieves 95% recall with 70% precision and reduces chimeric reads by ~90% while preserving 72–92% of true SVs. This improves SV validation rates 8–11 fold and eliminates false-positive inversion (INV) bias, restoring SV distributions to bulk-like profiles. Attention visualization reveals ChimeraLM focuses on junction regions with single-base precision, learning interpretable features applicable across sequencing technologies. By enabling confident SV detection at single-cell resolution, ChimeraLM addresses a fundamental data quality barrier in cancer genomics, developmental biology, and precision medicine. Available at <https://github.com/ylab-hi/ChimeraLM>.

Keywords: Whole Genome Amplification, Single Cell, Genomic Language Model, Structural Variation

047 **Main**

048

049 Single-cell genomics has revolutionized our resolution of biological heterogeneity,
050 enabling the discovery of rare cell types and the reconstruction of clonal evolution in
051 cancer and development [? ? ?]. However, a single cell contains only 6–7 picograms of
052 DNA—approximately two genome copies—posing significant technical challenges for
053 comprehensive genomic analysis [? ?]. Consequently, **WGA** remains an unavoidable
054 prerequisite, amplifying DNA 1,000- to 10,000-fold for high-coverage sequencing [?
055 ? ?]. While **WGA** provides necessary material for downstream analysis, it intro-
056 duces systematic errors that severely compromise genomic fidelity, particularly for **SV**
057 detection [? ? ?].

058 The most pernicious of these errors are chimera artifacts—artificial DNA con-
059 structs formed when highly processive polymerases, such as phi29 in **Multiple**
060 **Displacement Amplification (MDA)** [?], switch templates during amplification [? ? ?
061 ?]. These chimeras join discontinuous genomic loci into single molecules, mimicking
062 the structural signatures of biological **translocations (TRAs)** and **INVs** [?]. In long-
063 read sequencing, which is otherwise ideal for resolving complex **SVs**, chimeric reads
064 can constitute 42–76% of the **WGA** data [?], rendering standard **SV** callers unreli-
065 able [? ? ? ? ? ?]. Because these tools rely on alignment heuristics and coverage
066 deviations [? ?], they frequently misclassify artificial chimeras as genuine variants [?].

067 Distinguishing biological rearrangements from amplification artifacts remains a
068 major computational bottleneck. Current quality control methods rely on hand-
069 crafted features—such as read-pair orientation or localized coverage drops—that fail
070 to capture the sequence-intrinsic patterns of **WGA** errors [? ? ?]. This limitation
071 blocks the application of single-cell long-read sequencing in contexts where precision
072 is paramount, such as tracking somatic mosaicism or validating CRISPR off-target
073 effects.

074 We reasoned that **WGA** artifacts possess latent sequence motifs and structural
075 patterns distinct from genomic sequences, learnable without reliance on reference
076 alignment. Here, we present ChimeraLM, a platform-agnostic **Genomic Language**
077 **Model (GLM)** to identify and filter **WGA** artifacts with single-read resolution.

078 Leveraging advances in DNA foundation models [? ? ? ?], ChimeraLM treats
079 artifact detection as a sequence modeling task rather than an alignment problem. By
080 attending to long-range dependencies and contextual features within raw reads [? ? ?
081 ? ? ?], ChimeraLM achieves ~90% reduction in chimeric reads while preserving 72–
082 92% of true **SVs**. We demonstrate that this approach restores the fidelity of single-cell
083 **SV** calling, enabling robust characterization of genomic heterogeneity at the single-cell
084 level.

085

086 **Results**

087

088 **Overview of ChimeraLM workflow and model architecture**

089

090 Single-cell genomics relies on **WGA** to obtain sufficient DNA for sequencing (Fig. 1a).
091 The standard workflow includes single-cell isolation, DNA extraction, **WGA**, long-read
092 sequencing (e.g., **Oxford Nanopore Technologies (ONT)**), base calling, and alignment

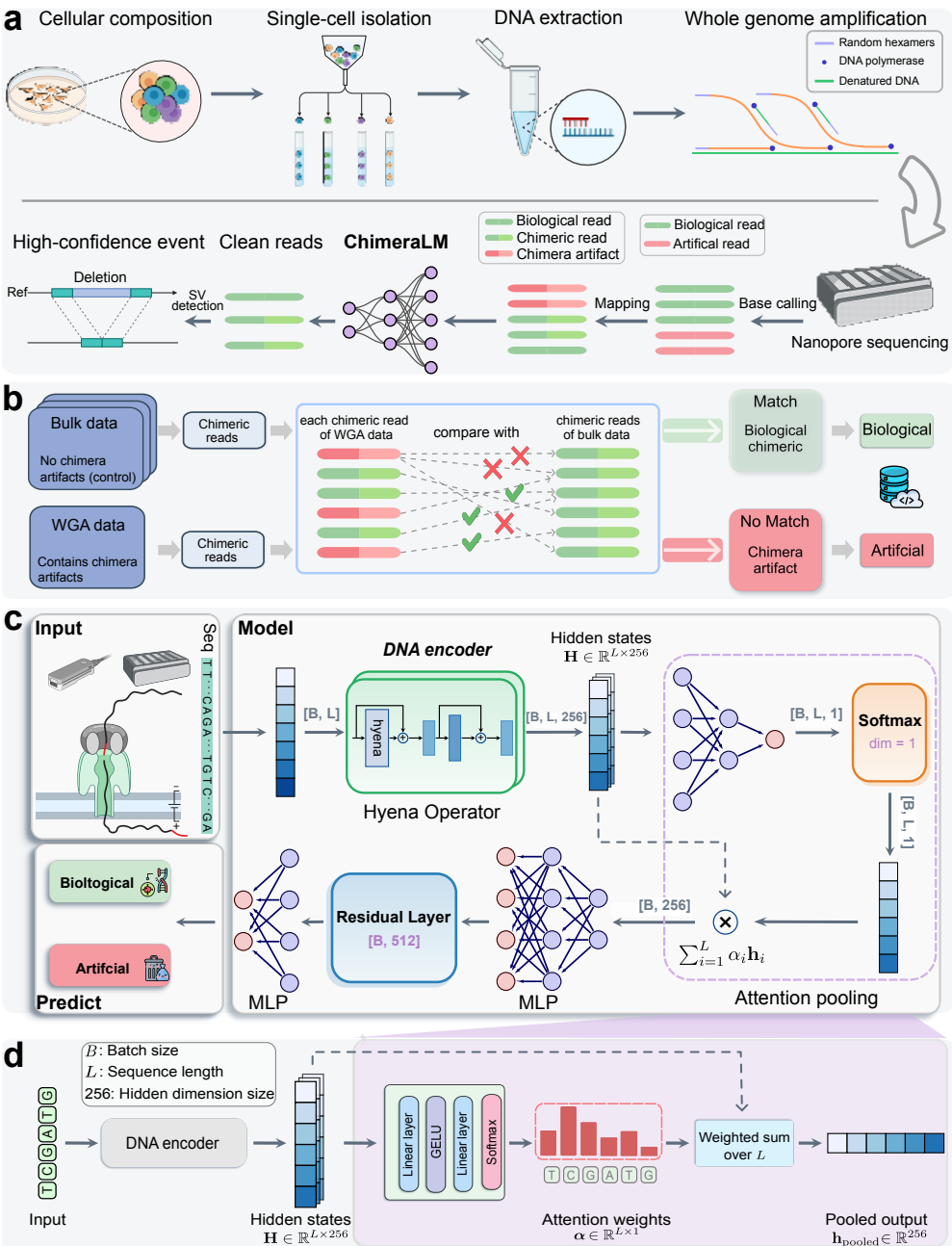


Fig. 1 ChimeraLM workflow and architecture for detecting WGA artifacts in single-cell sequencing. (a) Single-cell genomic workflow and ChimeraLM integration. Single cells are isolated, followed by DNA extraction and WGA for genome amplification. WGA generates chimeric artifacts (red) through template switching during amplification, alongside biological reads (green). After nanopore sequencing, ChimeraLM classifies chimeric reads as biological or artificial, enabling downstream SV detection on clean reads. (b) Ground truth label generation for supervised learning. Chimeric reads from WGA data are compared against all chimeric reads from bulk sequencing data of the same cell line. Reads that match bulk data are labeled as biological (green pathway), while non-matching reads are labeled as chimera artifacts (red pathway). This provides reliable training labels. (c) ChimeraLM architecture. Input DNA sequences (batch size B , sequence length L) are tokenized and encoded into hidden states $\mathbf{H} \in \mathbb{R}^{L \times 256}$ through a DNA encoder (HyenaDNA [?]). Hyena operators capture long-range dependencies in genomic sequences. Attention pooling aggregates position-specific features using learned weights. Residual and multilayer perceptron (MLP) layers process pooled features, and a softmax layer outputs binary classification probabilities for biological versus artificial reads. (d) Attention pooling mechanism detail. The DNA encoder (HyenaDNA) transforms input sequences into hidden state $\mathbf{H} \in \mathbb{R}^{L \times 256}$. Attention weights $\alpha \in \mathbb{R}^{L \times 1}$ are computed through linear layers, GELU activation, and softmax normalization, assigning importance scores to each nucleotide position. The weighted sum $\mathbf{h}_{\text{pooled}} = \sum_{i=1}^L \alpha_i \mathbf{h}_i$ produces the pooled output $\mathbf{h}_{\text{pooled}} \in \mathbb{R}^{256}$, compressing variable-length sequences into fixed-dimensional representations. Created with BioRender.com.

139 to the reference genome. During amplification, template-switching events introduce
140 artificial chimeric reads, resulting in alignment files containing a mixture of authentic
141 and artificial sequences that can mimic SVs and confound variant detection.

142 ChimeraLM integrates directly into this pipeline as a pre-processing filter, operat-
143 ing after read alignment but before SV detection (Fig. 1a). It evaluates each chimeric
144 read—sequences with multiple alignments to distant genomic locations—and classifies
145 it as either biological (genuine) or artificial (**WGA**-induced). This binary classifica-
146 tion enables retention of authentic genomic sequences while removing amplification
147 artifacts prior to variant calling.

148 Supervised training required a high-confidence labeled dataset (Fig. 1b; Extended
149 Data Fig. 1a). We constructed this dataset using sequencing data from the PC3
150 prostate cancer cell line, which provides both **WGA**-amplified and non-amplified (bulk)
151 genomic data. The key assumption is that bulk sequencing contains only genuine
152 genomic sequences, whereas **WGA** data includes both genuine and artificial chimeras.
153 Chimeric reads from the PC3 **WGA** PromethION dataset were systematically com-
154 pared against three independent bulk datasets (**ONT** PromethION, **ONT** MinION,
155 and **Pacific Biosciences (PacBio)**; see **Methods**). **WGA** reads whose chimeric structures
156 were absent from all three bulk datasets were labeled artificial; reads with structures
157 validated in one or more bulk datasets were labeled biological.

158 This labeling strategy identified 12,670,396 artificial chimeric reads (zero bulk
159 matches) and 293,180 biological chimeric reads from the **WGA** dataset (Extended
160 Data Fig. 1b). To construct the training dataset, we retained all 293,180 biological
161 reads, subsampled an equal number of artificial reads, and augmented the biological
162 class with 178,748 chimeric reads sampled directly from bulk sequencing data—genuine
163 structural rearrangements unaffected by amplification. This intentional class imbal-
164 ance prioritizes recall of true biological reads, minimizing loss of genuine variants
165 during filtering. The final dataset of 765,108 labeled reads was partitioned into training
166 (70%), validation (20%), and internal test (10%) sets using stratified splitting.

167 The ChimeraLM architecture (Fig. 1c) addresses three technical challenges inher-
168 ent to long-read classification: processing variable-length sequences spanning tens
169 of kilobases, maintaining single-nucleotide resolution to detect abrupt compositional
170 changes at chimeric junctions, and aggregating variable-length representations into
171 fixed-dimensional classification outputs. Input sequences are tokenized at single-
172 nucleotide resolution to preserve complete sequence information. The encoder employs
173 Hyena operators [?], which achieve subquadratic scaling with sequence length,
174 enabling analysis of full-length reads without fragmentation. We initialized the DNA
175 encoder with weights from HyenaDNA [?], a genomic foundation model pre-trained
176 on diverse DNA sequences. An attention pooling mechanism (Fig. 1d) aggregates
177 information across the entire read by computing learned, position-specific weights, pro-
178 ducing a fixed-dimensional representation. This representation is processed through
179 **MLP** layers with residual connections, and a final softmax layer outputs classification
180 probabilities.

181
182
183
184

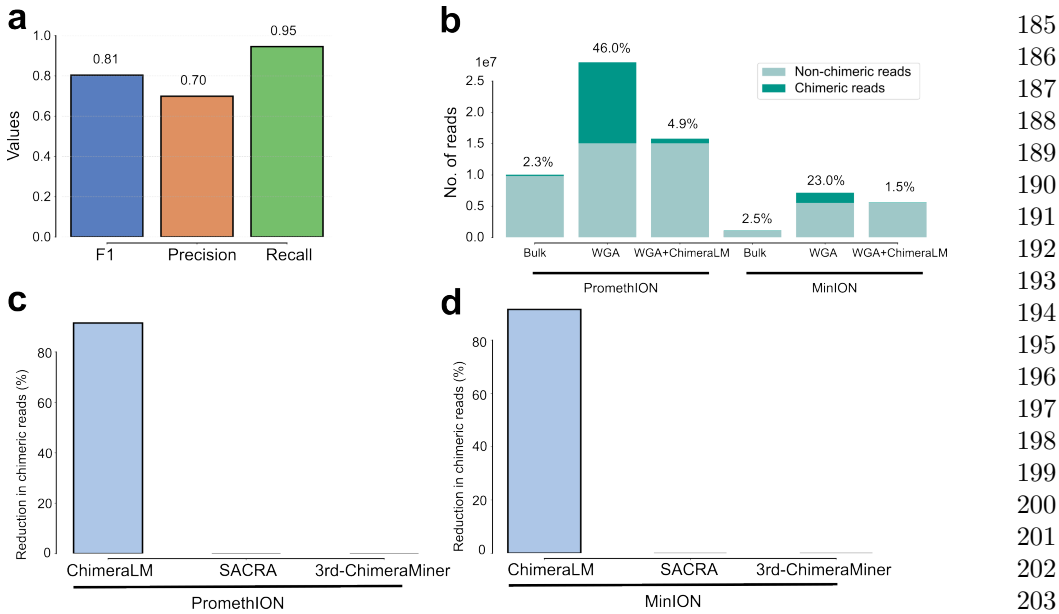


Fig. 2 ChimeraLM accurately identifies and removes WGA-induced chimeric artifacts.
 (a) Classification performance on held-out test data. ChimeraLM achieves high recall (0.95) in identifying chimera artifacts while maintaining acceptable precision (0.70), yielding an F1 score of 0.81 for binary classification of biological versus artificial sequences. (b) Chimeric read reduction across sequencing platforms. Stacked bars show the proportion of chimeric (dark teal) and non-chimeric (light teal) reads in bulk sequencing, WGA-amplified samples, and ChimeraLM-filtered WGA samples. Data from PC3 cell line sequenced on PromethION (left) and MinION (right) platforms demonstrate that ChimeraLM reduces chimeric read frequencies from 46.0% to 4.9% (PromethION) and from 23.0% to 1.5% (MinION), approaching bulk levels (2.3% and 2.5%, respectively). (c,d) Benchmarking against existing methods. ChimeraLM achieves approximately 90% reduction in chimeric reads on both PromethION (c) and MinION (d) platforms, whereas existing computational tools SACRA and 3rd-ChimeraMiner show no detectable reduction in chimeric content.

ChimeraLM achieves high accuracy and reduces artifacts to near-bulk levels across platforms

We evaluated ChimeraLM’s classification accuracy on the held-out test set, which comprised reads with known biological or artificial status (Fig. 2a). The model achieved an F1 score of 0.81, with recall of 0.95 indicating that 95% of chimeric artifacts were correctly identified—critical for minimizing downstream false-positive SV calls—and precision of 0.70 confirming that the majority of flagged reads were true artifacts.

We next assessed practical effectiveness on the full PC3 WGA datasets across PromethION and MinION platforms (Fig. 2b). Bulk sequencing established low baseline chimeric read rates (2.3% for PromethION; 2.5% for MinION), whereas WGA increased artifact load to 46.0% and 23.0%, respectively. After ChimeraLM filtering, chimeric content dropped to 4.9% (PromethION) and 1.5% (MinION)—10- to 15-fold reductions—while retaining 15.8 million and 5.6 million biological reads. This

185
186
187
188
189
190
191
192
193
194
195
196
197
198
199
200
201
202
203
204
205
206
207
208
209
210
211
212
213
214
215
216
217
218
219
220
221
222
223
224
225
226
227
228
229
230

231 restoration to near-bulk levels demonstrates effective separation of genuine reads from
232 **WGA**-induced artifacts.

233 We benchmarked ChimeraLM against SACRA [?] and 3rd-ChimeraMiner [?],
234 existing tools for detecting amplification-induced chimeras (Fig. 2c,d). ChimeraLM
235 achieved approximately 90% reduction in chimeric reads on both platforms; neither
236 SACRA nor 3rd-ChimeraMiner showed detectable reduction (0%).

237 The MinION results are particularly notable: this platform served as a com-
238 pletely independent test set, as the model was trained exclusively on PromethION
239 data. Effective generalization to MinION confirms that ChimeraLM learns universal
240 sequence-level features of **WGA**-induced artifacts rather than platform-specific sig-
241 natures. This cross-platform robustness suggests applicability beyond nanopore to other
242 long-read and short-read sequencing technologies.

243

244

245

246

247

248

249

250

251

252

253

254

255

256

257

258

259

260

261

262

263

264

265

266

267

268

269

270

271

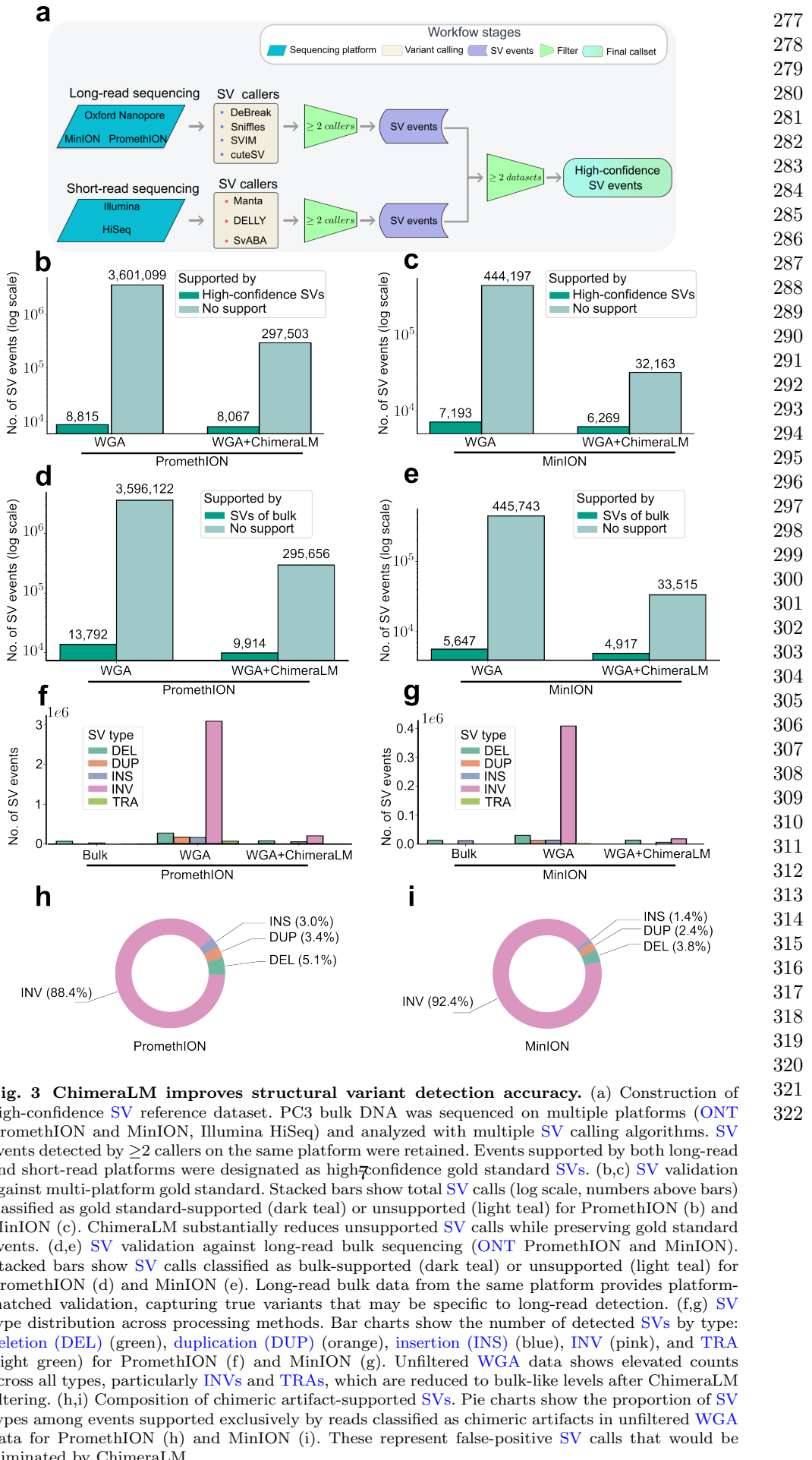
272

273

274

275

276



323 **ChimeraLM substantially reduces false-positive structural
324 variant calls**

325 To quantify ChimeraLM’s impact on **SV** calling accuracy, we compared variant calls
326 from unfiltered and ChimeraLM-filtered **WGA** data against two independent reference
327 standards (Fig. 3).

328 We first established a high-confidence gold standard **SV** dataset from bulk PC3
329 DNA sequenced on multiple platforms (**ONT** PromethION, **ONT** MinION, and Illu-
330 mina HiSeq) and analyzed with multiple **SV** callers (Fig. 3a; Extended Data Table 1).
331 **SVs** detected by ≥ 2 callers on the same platform and supported by both long-read
332 and short-read data were retained as gold-standard events.

333 Unfiltered **WGA** data contained extensive false-positive **SVs** (Fig. 3b,c). On Prome-
334 thION, raw **WGA** produced 3.6 million **SV** calls, of which only 8,815 (0.24%) matched
335 gold standard events—over 99% were artifacts. After ChimeraLM filtering, total calls
336 dropped to 305,570 while retaining 8,067 gold standard events (91.5% of true variants),
337 raising the validation rate to 2.64% (11-fold improvement). MinION data showed simi-
338 lar improvements: calls reduced from 451,390 to 38,432 with validation rate increasing
339 from 1.59% to 16.3% (10-fold improvement) while retaining 87.2% of true variants.

340 We next performed platform-matched validation, comparing **WGA**-derived **SV** calls
341 against long-read bulk sequencing from the same platform (Fig. 3d,e). This reference
342 captures true **SVs** that may be missed by short-read data, providing a more inclusive
343 measure of recall. ChimeraLM increased validation rates from 0.38% to 3.24% on
344 PromethION (8.5-fold improvement) and from 1.25% to 12.79% on MinION (10-fold
345 improvement), while retaining 71.9% and 87.1% of bulk-supported events, respectively.

346 Together, ChimeraLM reduces false-positive **SV** calls by 8–11 fold while preserving
347 72–92% of true variants, substantially enhancing the signal-to-noise ratio in single-cell
348 **SV** discovery.

350
351 **ChimeraLM restores unbiased SV-type distributions**

352 Amplification artifacts can distort the apparent spectrum of **SVs**. We compared **SV**
353 type distributions across bulk, unfiltered **WGA**, and ChimeraLM-filtered datasets
354 (Fig. 3f,g). Bulk sequencing showed balanced proportions of **DELs**, **DUPs**, **INSS**,
355 **INVs**, and **TRAs**. Unfiltered **WGA** data exhibited dramatic overrepresentation of
356 **INVs** on both platforms, consistent with amplification artifacts. After ChimeraLM fil-
357 tering, **SV** distributions were restored toward bulk-like profiles: excessive **INVs** were
358 markedly reduced while other categories remained stable, reflecting selective removal
359 of artifact-supported **INVs** rather than indiscriminate loss of genuine signals.

360 To characterize the artifact composition, we analyzed **SV** calls supported exclu-
361 sively by reads classified as chimera artifacts (Fig. 3h,i). These artifact-supported
362 events were dominated by **INVs**, comprising 88.4% on PromethION and 92.4% on
363 MinION—consistent with template-switching junctions producing inversion-like align-
364 ment signatures. Smaller fractions of **DELs** (5.1% and 3.8%), **DUPs** (3.4% and 2.4%),
365 and **INSS** (3.0% and 1.4%) indicate that **WGA**-induced chimeras can mimic diverse
366 **SV** categories.

367
368

Although **INVs** predominate, the presence of other **SV** types among chimeric events indicates that comprehensive filtering—rather than inversion-specific correction—is essential for accurate **SV** detection. By restoring biologically representative **SV** type distributions, ChimeraLM enables robust and interpretable characterization of **SV** in single cells.

369
370
371
372
373
374
375
376
377
378
379
380
381
382
383
384
385
386
387
388
389
390
391
392
393
394
395
396
397
398
399
400
401
402
403
404
405
406
407
408
409
410
411
412
413
414

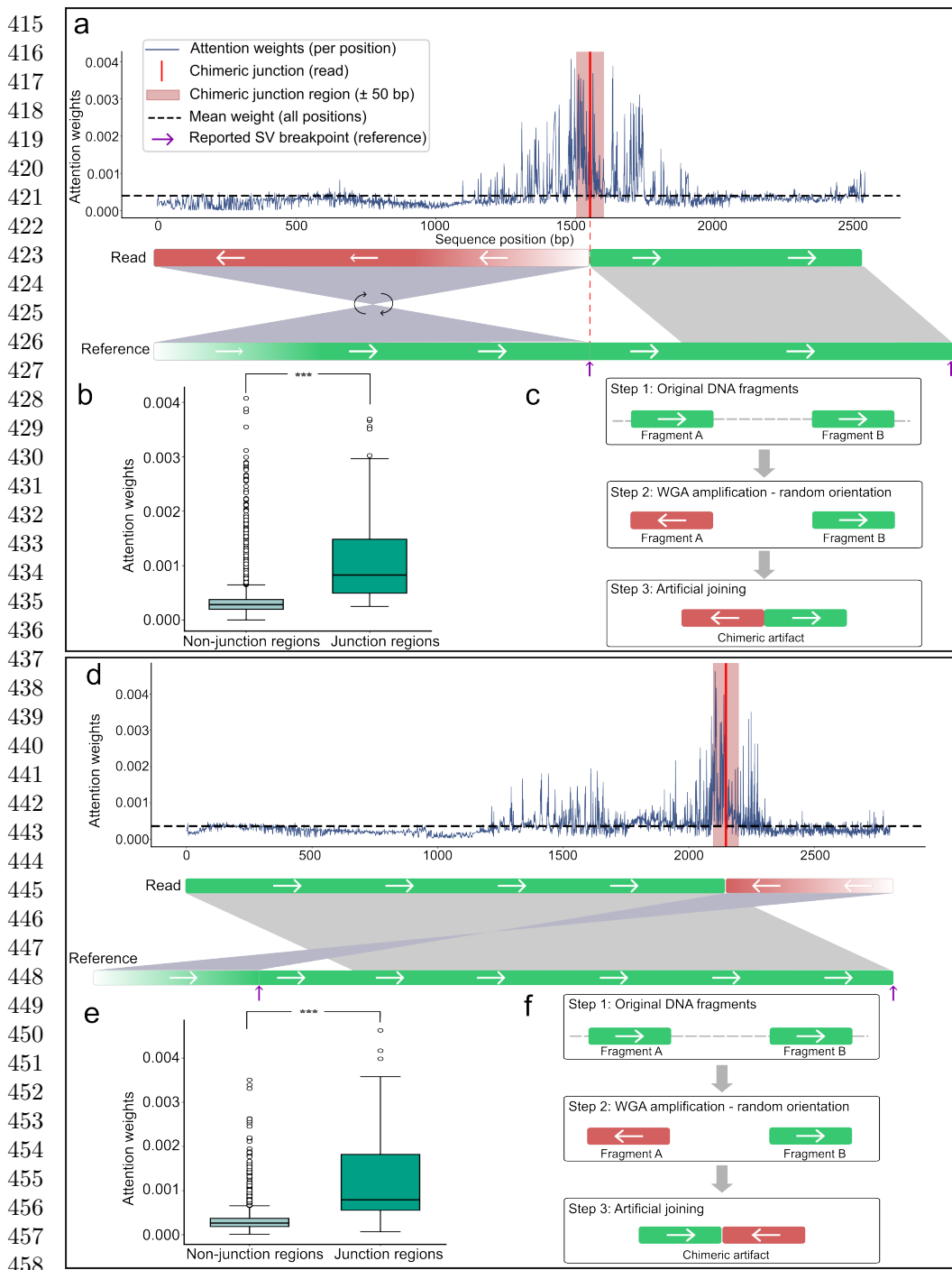


Fig. 4 ChimeraLM attention weights can localize to chimeric junction regions.

(a,d) Attention weight profiles for two representative chimeric reads. Upper panels show attention weights per sequence position (blue line) and mean attention (dashed line). Red vertical lines mark chimeric junction positions, with pink shading indicating junction region (± 50 bp). Purple arrows show reported SV breakpoints. Lower panels illustrate read alignments: reads (top bars) show orientation transitions at junctions (green = forward, red = reverse-complemented, arrows indicate strand), while reference genome (bottom bars) maintains continuous forward orientation. Gray regions connect aligned segments. (b,e) Quantitative attention analysis. Box plots show significantly elevated attention weights in junction region versus non-junction regions for both examples ($p = 5.3 \times 10^{-14}$ and $p = 6.8 \times 10^{-15}$, respectively; Wilcoxon rank-sum test). (c,f) Proposed chimera formation mechanisms. Step 1: Original DNA fragments from distant genomic loci exist in forward orientation. Step 2: During WGA, one or both fragments may undergo random reverse-complementation. Step 3: Template switching joins the fragments with discordant orientations, creating chimeric artifacts. The two examples illustrate different orientation patterns (forward-to-reverse vs reverse-to-forward transitions) arising from random strand selection during amplification.

Attention visualization reveals interpretable classification features	461
	462
	463
	464
	465
	466
	467
	468
	469
	470
	471
	472
	473
	474
	475
	476
	477
	478
	479
	480
	481
	482
	483
	484
	485
	486
	487
	488
	489
	490
	491
	492
	493
	494
	495
	496
	497
	498
	499
	500
	501
	502
	503
	504
	505
	506

We investigated whether ChimeraLM’s attention mechanism highlights biologically meaningful regions (Fig. 4). For representative chimeric reads, attention weight profiles showed low baseline values across most positions but pronounced peaks at junction regions where template switching joins DNA fragments from distinct genomic loci (Fig. 4a,d). These peaks coincided with alignment breakpoints characterized by orientation changes between adjacent read segments—the defining signature of WGA-induced artifacts.

Attention weights within junction regions (± 50 bp) were significantly higher than in non-junction regions (Wilcoxon rank-sum test, $P = 5.3 \times 10^{-14}$ and $P = 6.8 \times 10^{-15}$; Fig. 4b,e), indicating that ChimeraLM learns mechanistically relevant features rather than spurious correlations.

Schematic reconstruction of the amplification process supports this interpretation (Fig. 4c,f). During WGA, DNA fragments from distant loci undergo random strand orientation changes before being joined by template switching, producing artificial junctions with discordant orientations that generate inversion-like alignment signatures. The model’s attention peaks effectively capture these orientation discontinuities, localizing chimeric junctions at single-nucleotide resolution.

Discussion

WGA has enabled genomic analysis from single cells but introduces chimeric artifacts that compromise SV detection. ChimeraLM addresses this challenge through sequence-level classification of biological versus artificial reads, substantially improving SV calling accuracy before downstream analysis. This upstream filtering strategy—removing problematic sequences at the read level rather than correcting errors post hoc—provides a practical solution for single-cell genomics laboratories.

Our results demonstrate several key advantages of ChimeraLM for long-read single-cell sequencing. The method achieves approximately 90% reduction in chimeric reads across nanopore platforms while retaining 72–92% of true SVs. It reduces false-positive SV calls by 8–11 fold, enabling researchers to focus on biologically relevant variants without manually filtering thousands of artifacts. Moreover, ChimeraLM performs consistently across PromethION and MinION without platform-specific retraining, indicating that it captures generalizable sequence features of WGA-induced chimeras. These results underscore the model’s robustness across diverse datasets and sequencing conditions.

ChimeraLM’s effectiveness reflects the ability of deep learning models to capture complex sequence patterns that are difficult to encode in rule-based filters. Traditional quality control methods rely on predefined metrics such as mapping quality or read depth [? ?], which may not effectively distinguish chimeric artifacts from biological reads. By learning directly from sequence data, ChimeraLM discovers subtle compositional and structural features that differentiate authentic genomic sequences from amplification artifacts. Furthermore, the model offers interpretability through attention visualization, allowing researchers to examine which sequence regions drive

507 classification. Attention weights can concentrate sharply at junctions where template
508 switching joins DNA fragments from distinct loci, matching the known mechanism of
509 chimera formation. Some reads show more diffuse attention distributions, suggesting
510 that ChimeraLM integrates multiple complementary cues—such as junction orien-
511 tation, compositional biases, and local sequence context—to classify diverse artifact
512 types. This interpretability builds confidence in the model’s predictions and provides
513 a lens for probing the molecular processes underlying amplification-induced artifacts.

514 The improved reliability of **SV** detection has direct implications for single-cell
515 genomics. Studies of chromosomal instability, clonal evolution, and **SV** burden in indi-
516 vidual cells have long been constrained by high false-positive rates in **WGA** data [?
517 ?]. ChimeraLM enables more confident identification of genuine **SVs**, supporting
518 research in cancer genomics, developmental biology, and aging where single-cell resolu-
519 tion is essential for understanding cellular heterogeneity. Although the current model
520 processes reads independently, integrating additional contextual features—such as cov-
521 erage, mate-pair, or phasing information—could further enhance accuracy. **Graphics**
522 **Processing Unit (GPU)** resources are recommended for large-scale datasets, while **Central**
523 **Processing Unit (CPU)** inference remains feasible for smaller studies; runtime
524 optimization and model compression may improve accessibility for broader use.

525 Future work should prioritize validation across diverse biological and technical con-
526 texts. First, testing on multiple cell types (primary, stem, or immune cells) and **WGA**
527 protocols (**Multiple Annealing and Looping-based Amplification Cycles (MALBAC)**,
528 **Linear Amplification via Transposon Insertion (LIANTI)**, **Primary Template-directed**
529 **Amplification (PTA)**) will establish biological generalizability. Second, validation on
530 additional sequencing platforms—including PacBio HiFi, Illumina linked-reads, and
531 emerging long-read technologies—will confirm the platform-agnostic design prin-
532 ciple. The sequence-level approach suggests ChimeraLM should transfer effectively
533 to any platform, though platform-specific fine-tuning may optimize performance.
534 Third, the interpretability of attention-based models could be leveraged to investi-
535 giate mechanisms of chimera formation: large-scale analysis of attention patterns
536 may reveal recurrent sequence motifs or genomic contexts associated with template
537 switching, guiding the development of improved amplification protocols. More broadly,
538 ChimeraLM illustrates the potential of **GLMs** for data quality control applications [?
539 ?]. Architectural innovations such as the Hyena operator for efficient long-range mod-
540 eling [?] may have utility beyond chimera detection, addressing challenges such as
541 contamination, adapter artifacts, and systematic sequencing errors across multiple
542 platforms.

543 Looking ahead, ChimeraLM’s framework could extend beyond single-cell genomics
544 to address quality control challenges in other amplification-dependent technologies,
545 including cell-free DNA analysis, ancient DNA studies, and metagenomic sequencing
546 from low-biomass samples. The model’s interpretability through attention visual-
547 ization also opens opportunities for mechanistic studies of polymerase fidelity and
548 template-switching dynamics across different amplification protocols. Furthermore,
549 integration with emerging single-cell multi-omics platforms could enable simultaneous
550 quality control across genomic, transcriptomic, and epigenomic data layers, providing
551 a unified framework for artifact detection in complex single-cell experiments.

552

ChimeraLM thus provides a practical and interpretable framework for improving long-read single-cell genomic data quality. By removing WGA-induced chimeric artifacts at the read level and revealing the mechanistic features that drive them, the method not only enhances SV detection reliability but also deepens understanding of amplification-induced bias in single-cell genomics.

Methods

Cell culture, single-clone preparation, and nanopore sequencing

Cell culture and single-clone establishment

PC3 prostate cancer cells (ATCC® CRL-1435™) were cultured in RPMI-1640 medium supplemented with 10% fetal bovine serum and 1% penicillin–streptomycin at 37 °C with 5% CO₂. To minimize biological heterogeneity, a monoclonal population was established by serial dilution in 96-well plates, ensuring that each culture originated from a single cell. Mycoplasma contamination was routinely tested and confirmed negative prior to DNA extraction.

DNA extraction and whole-genome amplification

From the monoclonal population, two types of DNA samples were prepared: a bulk (non-amplified) control and ten single-cell MDA-amplified genomes. Bulk high-molecular-weight DNA was extracted using the Monarch® HMW DNA Extraction Kit for Cells & Blood (New England Biolabs). Individual cells were isolated using 1CellDish-60 mm (iBiochips) and amplified using the REPLI-g Advanced DNA Single Cell Kit (Qiagen) following the manufacturer's protocol. DNA concentration and fragment integrity were assessed with a Qubit 4 fluorometer and Agilent TapeStation (DNA 1000/5000 ScreenTape). Only samples meeting quality standards were used for library construction.

Nanopore library preparation and sequencing

Sequencing libraries were prepared using the ONT Ligation Sequencing Kit V14 (SQK-LSK114) and sequenced on MinION Mk1C or PromethION P2 Solo devices with R10.4.1 flow cells according to the manufacturer's genomic DNA workflow. Because all single-cell samples originated from the same monoclonal lineage, observed differences between amplified and bulk data primarily reflect MDA-induced artifacts rather than biological variation, providing a controlled experimental setting for downstream analyses.

Basecalling and read processing

Raw signal files (POD5) were basecalled using Dorado v0.5.0 with the high-accuracy model dna_r10.4.1_e8.2_400bps_hac@v4.3.0 [?]. Reads with mean quality < 10 or length < 500 bp were removed. Residual adapters and concatemers were trimmed using Cutadapt v4.0 [?] in two-pass error-tolerant mode. Cleaned reads were aligned to the GRCh38.p13 reference genome using minimap2 v2.26 (map-ont preset) [?]. Resulting BAM files were sorted and indexed with SAMtools v1.16 [?]. Read length

599 and mapping statistics were calculated using NanoPlot v1.46.1 [?]. All samples were
600 processed under identical parameters to ensure consistency across datasets.

601

602 *Chimeric read identification*

603 Chimeric reads were identified based on the presence of supplementary alignments in
604 BAM files using the [Supplementary Alignment \(SA\)](#) tag. The [SA](#) tag indicates that
605 a read has additional alignments beyond the primary alignment, which is character-
606 teristic of chimeric sequences that map to multiple distant genomic locations. To ensure
607 accurate identification, we applied stringent filtering criteria: reads were classified as
608 chimeric only if they (1) were not unmapped, (2) contained the [SA](#) tag, (3) were not
609 secondary alignments, and (4) were not supplementary alignments themselves. This
610 filtering approach ensures that only primary alignments with supplementary mapping
611 evidence are considered chimeric, avoiding double-counting of the same chimeric event
612 and excluding low-quality or ambiguous alignments. Reads without the [SA](#) tag (single
613 continuous alignments) were classified as non-chimeric. This approach leverages the
614 standard BAM format specification to reliably identify reads with complex alignment
615 patterns.

616

617 **Training data construction**

618

619 *Data generation and sources*

620 To construct the training dataset, we generated [WGA](#) and bulk sequencing data from
621 PC3 cells. The [WGA](#) sample was amplified and sequenced on the PromethION P2 plat-
622 form ([ONT](#)), while three independent bulk datasets were produced from non-amplified
623 genomic DNA: bulk PromethION P2, bulk MinION Mk1c ([ONT](#)), and bulk PacBio.
624 These bulk datasets represent authentic biological sequences free from amplification-
625 induced artifacts. In contrast, [WGA](#) sequencing includes both genuine genomic reads
626 and artificial chimeras introduced during the amplification process. An additional
627 [WGA](#) dataset sequenced on the MinION Mk1c platform was reserved exclusively as
628 an independent test set for cross-platform evaluation.

629

630 *Ground truth annotation and class definition*

631 Ground truth labels were established by systematically comparing chimeric reads from
632 the [WGA](#) PromethION P2 dataset against those from the three bulk datasets. For
633 each [WGA](#) chimeric read, all alignment segments—defined by their genomic start
634 and end coordinates—were compared to the corresponding segments of bulk chimeric
635 reads. A [WGA](#) read was labeled as biological if every segment matched at least one
636 bulk chimeric read within a 1 kb positional tolerance, indicating that the structural
637 configuration is also present in non-amplified DNA. Reads lacking any matching pat-
638 tern across all bulk datasets were labeled as artificial chimeras, presumed to arise
639 from the amplification process. To ensure balanced class representation, additional
640 chimeric reads were randomly sampled from the bulk datasets and labeled as biologi-
641 cal, as these reads originate from genuine genomic rearrangements such as true [SVs](#).
642 The final labeled dataset combined the annotated [WGA](#) PromethION P2 reads with
643

644

the subsampled bulk chimeric reads and was subsequently partitioned into training, validation, and test sets as described below.

Dataset partitioning and cross-platform validation

The combined labeled dataset, derived from **WGA** PromethION P2 and bulk sequencing data, was divided into training (70%), validation (20%), and internal test (10%) sets using stratified random sampling to maintain class balance. These subsets were used respectively for model training, hyperparameter tuning, and performance evaluation on data from the same sequencing platform.

To evaluate cross-platform generalization, the complete **WGA** MinION Mk1c dataset was reserved as an independent external test set. This dataset, generated on a different nanopore platform, was never used during model training or internal testing. This two-level evaluation design allowed us to test whether ChimeraLM captures general sequence features of amplification-induced chimeras rather than platform-specific artifacts.

Model architecture

DNA encoder

ChimeraLM employs the pre-trained HyenaDNA model [?] as its DNA encoder. This model was pre-trained on large-scale genomic data and provides robust sequence representations. DNA sequences are tokenized at single-nucleotide resolution, with each base (A, C, G, T, N) mapped to a unique integer token (7, 8, 9, 10, 11, respectively). Special tokens include [CLS]=0, [PAD]=4, and others for sequence processing. Input sequences are truncated at 32,768 bp or padded to enable batch processing.

For a tokenized input sequence $\mathbf{x} \in \mathbb{Z}^L$, the HyenaDNA generates contextualized hidden representations:

$$\mathbf{H} = \text{HyenaDNA}(\mathbf{x}) \in \mathbb{R}^{L \times 256}$$

where $\mathbf{H} = (\mathbf{h}_1, \mathbf{h}_2, \dots, \mathbf{h}_L)$ represents position-wise hidden states with dimension 256. The Hyena operators [?] efficiently capture both local sequence motifs and long-range dependencies essential for distinguishing biological sequences from chimeric artifacts.

Attention pooling

To aggregate variable-length sequence representations into fixed-size vectors, ChimeraLM implements attention-based pooling. For hidden states $\mathbf{H} \in \mathbb{R}^{L \times 256}$, attention weights are computed through a two-layer network:

$$\mathbf{e} = \text{GELU}(\text{Linear}_{256 \rightarrow 256}(\mathbf{H})) \in \mathbb{R}^{L \times 256}$$

$$\mathbf{s} = \text{Linear}_{256 \rightarrow 1}(\mathbf{e}) \in \mathbb{R}^{L \times 1}$$

$$\boldsymbol{\alpha} = \text{softmax}(\mathbf{s}) \in \mathbb{R}^{L \times 1}$$

691 The pooled representation is the weighted sum of hidden states:
 692
 693 $\mathbf{h}_{\text{pooled}} = \sum_{i=1}^L \alpha_i \mathbf{h}_i \in \mathbb{R}^{256}$
 694
 695
 696 This mechanism assigns learned importance weights to each sequence position,
 697 enabling the model to focus on informative regions while accommodating natural
 698 variability in read lengths.
 699

700 ***Classification head***
 701 The pooled representation is processed through a **MLP** with residual connections. The
 702 first layer expands dimensionality:
 703

704 $\mathbf{f}_1 = \text{Dropout}_{0.1}(\text{GELU}(\text{Linear}_{256 \rightarrow 512}(\mathbf{h}_{\text{pooled}}))) \in \mathbb{R}^{512}$
 705
 706 Subsequent residual blocks with input $\mathbf{f}_{\text{in}} \in \mathbb{R}^{512}$ compute:
 707
 708 $\mathbf{f}_{\text{out}} = \text{Dropout}_{0.1}(\text{Linear}_{512 \rightarrow 512}(\text{GELU}(\text{Linear}_{512 \rightarrow 512}(\mathbf{f}_{\text{in}})))) + \mathbf{f}_{\text{in}}$
 709
 710 where the skip connection enables stable gradient flow during training. The final layer
 711 produces binary classification logits:
 712

713 $\mathbf{z} = [z_0, z_1] = \text{Linear}_{512 \rightarrow 2}(\mathbf{f}_{\text{final}}) \in \mathbb{R}^2$
 714
 715 where z_0 and z_1 represent logits for biological and artificial chimeric classes, respec-
 716 tively. During inference, the predicted class is $\hat{y} = \text{argmax}_{i \in \{0,1\}} z_i$.
 717

718 ***Model summary***
 719 The complete ChimeraLM pipeline processes DNA sequences through: (1) single-
 720 nucleotide tokenization, (2) HyenaDNA backbone encoding to generate contextualized
 721 representations, (3) attention pooling to aggregate position-specific features, (4) **MLP**
 722 layers with residual connections to learn classification features, and (5) binary classi-
 723 fication output. The entire model is trained end-to-end using labeled **WGA** and bulk
 724 sequencing data.
 725

726
 727 **Model training and optimization**
 728
 729 ***Training configuration***
 730 ChimeraLM was trained using PyTorch [?] and PyTorch Lightning [?] frameworks.
 731 Input sequences were tokenized using the tokenizer with maximum sequence length of
 732 32,768 bp. Sequences longer than this threshold were truncated; shorter sequences were
 733 padded to enable batch processing. Training employed mixed-precision computation
 734 (bf16) to accelerate training while maintaining numerical stability.
 735
 736

Optimization procedure	737
We used the AdamW optimizer [?] with learning rate $\eta = 1 \times 10^{-4}$ and weight decay $\lambda = 0.01$. AdamW implements adaptive learning rates with decoupled weight decay, combining the benefits of Adam optimization with proper L2 regularization.	738
A ReduceLROnPlateau scheduler dynamically adjusted the learning rate based on validation loss, reducing it by a factor of 0.1 when no improvement occurred for 10 consecutive epochs. Early stopping with patience of 10 epochs prevented overfitting by terminating training when validation performance plateaued. A fixed random seed (12345) ensured reproducibility across training runs.	739
	740
	741
	742
	743
	744
	745
	746
	747
	748
	749
	750
	751
	752
	753

The training objective used cross-entropy loss for binary classification. For a training example with true class label $y \in \{0, 1\}$ and model logits $\mathbf{z} = [z_0, z_1]$, the loss is:

$$\mathcal{L}(\mathbf{z}, y) = -\log \left(\frac{\exp(z_y)}{\exp(z_0) + \exp(z_1)} \right) = -z_y + \log(\exp(z_0) + \exp(z_1))$$

where z_0 and z_1 represent logits for biological and artificial chimeric classes, respectively.

Training implementation

Training used batch size of 16 sequences with 30 parallel data loading workers. GPU acceleration was employed for efficient processing, with training typically requiring 96–120 hours depending on dataset size. Model checkpointing saved the best-performing model based on validation metrics. Configuration management used Hydra [?] to enable reproducible experimentation.

Model evaluation

Performance was monitored using accuracy, precision, recall, and F1 score on the validation set after each epoch:

$$\text{Precision} = \frac{\text{TP}}{\text{TP} + \text{FP}}, \quad \text{Recall} = \frac{\text{TP}}{\text{TP} + \text{FN}}$$

$$\text{F1} = \frac{2 \times \text{Precision} \times \text{Recall}}{\text{Precision} + \text{Recall}}, \quad \text{Accuracy} = \frac{\text{TP} + \text{TN}}{\text{TP} + \text{TN} + \text{FP} + \text{FN}}$$

where TP (true positives) are chimeric reads correctly classified as artificial, TN (true negatives) are biological reads correctly classified as biological, FP (false positives) are biological reads misclassified as artificial, and FN (false negatives) are chimeric reads misclassified as biological. Final model selection was based on best validation performance as determined by early stopping.

Model inference and application

Inference pipeline

To apply ChimeralLM to new WGA sequencing data, the model takes a BAM file as input. Chimeric reads are identified using SA tags and filtered to exclude unmapped, secondary, or supplementary alignments. Each chimeric read sequence is tokenized

783 using the tokenizer (maximum length 32,768 bp, with truncation or padding as
784 needed). The trained model processes sequences in batches, generating two logits
785 $[z_0, z_1]$ for each read corresponding to biological and artificial chimeric classes. Clas-
786 sification is determined by $\hat{y} = \text{argmax}(z_0, z_1)$. ChimeraLM outputs a filtered BAM
787 file containing only reads classified as biological, which can be directly used for
788 downstream analyses including **SV** calling.

789

790 **Performance evaluation**

791

792 *Test set evaluation*

793 Final model performance was evaluated on the held-out test set and the independent
794 MinION Mk1c dataset. Metrics (precision, recall, F1 score, accuracy) were computed
795 as described in the training section, where true positives represent chimeric reads
796 correctly classified as artificial and true negatives represent biological reads correctly
797 classified as biological.

798

799 *SV calling*

800 **SVs** were called using multiple tools to ensure comprehensive detection. For long-
801 read data (ONT PromethION P2 and MinION Mk1c), we used Sniffles v2.5 [? ?],
802 DeBreak v1.2 [?], SVIM v2.0.0 [?], and cuteSV v2.1.1 [?]. For short-read data of the
803 PC3 cell line, we used both the CCLE Illumina whole-genome sequencing dataset and
804 the PRJNA361315 Illumina WGS dataset, processed with Manta v1.6.0 [?], DELLY
805 v1.5.0 [?], and SvABA v1.1.0 [?]. All tools were executed with default recommended
806 parameters.

807

808 *Gold standard SV dataset construction*

809 A high-confidence gold standard **SV** dataset was generated from bulk PC3 sequencing
810 data to evaluate the impact of ChimeraLM on **SV** detection accuracy (Fig. 3a). All
811 **SV** comparison and breakpoint correction were performed using OctopuSV v0.2.3 [?].
812 We used four datasets: bulk MinION Mk1c, bulk PromethION P2, the CCLE Illumina
813 WGS dataset, and the PRJNA361315 Illumina WGS dataset. Within each dataset, **SV**
814 events supported by at least two independent callers were retained. Variants supported
815 by two or more datasets were designated as gold standard **SVs** for benchmarking.
816

817

818 *SV benchmarking analysis*

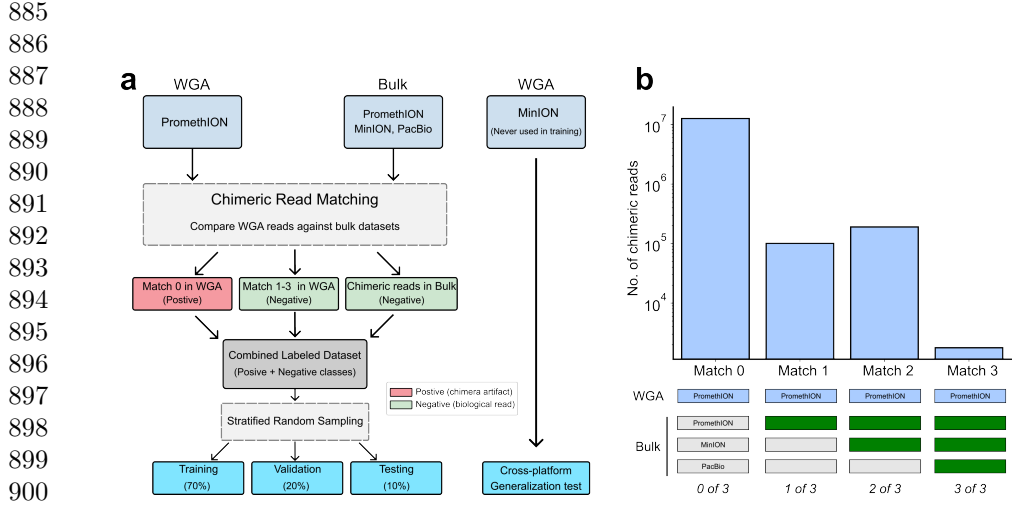
819 To assess the impact of ChimeraLM on **SV** calling accuracy, we compared **SV** calls from
820 unfiltered **WGA** data and ChimeraLM-filtered **WGA** data against two references: (1)
821 the stringent multi-platform gold standard dataset, and (2) platform-matched long-
822 read bulk sequencing data. Benchmarking was performed using Truvari v4.2.2 [?]
823 with default parameters. **SVs** were considered supported if they matched reference
824 variants within the defined breakpoint tolerance. Validation rates were calculated as
825 the proportion of called **SVs** supported by the reference. This dual benchmarking
826 strategy quantifies both improvements in detecting high-confidence multi-platform
827 **SVs** and the retention of platform-specific true variants.

828

Benchmarking against existing methods	829
ChimeraLM was compared to two existing computational methods for detecting amplification-induced chimeric artifacts: SACRA [?] (GitHub commit 9a2607e) and 3rd-ChimeraMiner [?] (GitHub commit 04b5233). Both tools were applied to WGA data from PromethION P2 and MinION Mk1c platforms using default parameters as recommended in their documentation. Performance was evaluated by measuring the percentage reduction in chimeric reads relative to unprocessed WGA data. Chimeric reads were identified using WGA tag-based alignment criteria (reads with SA tags indicating split alignments), and reduction rates were calculated as the proportion of chimeric reads removed by each method.	830 831 832 833 834 835 836 837 838 839 840 841 842 843 844 845 846 847 848 849 850 851 852 853 854 855 856 857 858 859 860 861 862 863 864 865 866 867 868 869 870 871 872 873 874
Attention weight analysis	841
To investigate ChimeraLM’s interpretability, we analyzed attention weights from the pooling mechanism for representative chimeric reads. Attention weights indicate the relative importance assigned to each sequence position during classification. For selected reads, we extracted per-position attention weights and visualized them alongside read alignments to identify whether the model focuses on mechanistically relevant regions.	842 843 844 845 846 847 848 849 850 851 852 853 854 855 856 857 858 859 860 861 862 863 864 865 866 867 868 869 870 871 872 873 874
Chimeric junction positions were identified from alignment data (defined by breakpoints in SA tags). A window of ± 50 bp surrounding each junction was designated as the junction region. Attention weights within junction region were compared to non-junction regions using the Wilcoxon rank-sum test [?], with statistical significance assessed at $p < 0.001$.	842 843 844 845 846 847 848 849 850 851 852 853 854 855 856 857 858 859 860 861 862 863 864 865 866 867 868 869 870 871 872 873 874
Data visualization	854
Figures were generated using Python with Matplotlib [?] and Seaborn [?].	855
Computing resources	855
Computations were performed on a High Performance Computing (HPC) server with 64-core Intel Xeon Gold 6338 CPU, 256 GB RAM, and two NVIDIA A100 GPUs (80 GB memory each).	856 857 858 859 860 861 862 863 864 865 866 867 868 869 870 871 872 873 874
Supplementary information.	863
Acknowledgements. We thank Tingyou Wang for guidance on figure preparation. This project was supported in part by NIH grants R35GM142441 and R01CA259388 awarded to RY.	864 865 866 867 868 869 870 871 872 873 874
Declarations	869
Author Contributions. YL, QG and RY designed the study. YL and QG performed the analysis. QG performed the experiments. YL and QG designed and implemented the model. YL built the command-line tool and documentation. YL, QG and RY wrote the manuscript. RY supervised this work.	870 871 872 873 874

875
876 **Extended Data Table 1** Sequencing and alignment statistics of PC3

Sample	Platform	Reads ($\times 10^6$)	Total bases (Gb)	Total aligned bases (Gb)	Fraction aligned	Mean length (bp)	Mean quality (Q)	Average identity (%)
WGA	MinION	9.11	14.6	10.4	0.7	1,603	14.3	97.6
WGA	PromethION	44.69	128.2	69.2	0.5	2,869	14.5	96.1
Bulk	MinION	0.97	8.1	7.1	0.9	8,310	17.2	97.3
Bulk	PromethION	8.00	69.9	62.4	0.9	8,732	18.5	97.7



922 **Data Availability.** The raw sequencing data generated in this study have been
923 deposited in the NCBI Sequence Read Archive (SRA) under BioProject accession

PRJNA1354861. The dataset includes Oxford Nanopore long-read whole-genome sequencing of PC3 prostate cancer cells and MDA-amplified single-cell derivatives. The individual SRA accessions are as follows: PC3 bulk (MinION Mk1C), SRR35904028; PC3 bulk (PromethION P2), SRR35904029; PC3 10-cell WGA (MinION Mk1C), SRR35904026; PC3 10-cell WGA (PromethION P2), SRR35904027. We can access the data at the following link: https://dataview.ncbi.nlm.nih.gov/object/PRJNA1354861?reviewer=viej6cv6mgbli3n7a9a5k1bsb3	921 922 923 924 925 926 927 928 929 930 931 932 933 934 935 936 937 938 939 940 941 942 943 944 945 946 947 948 949 950 951 952 953 954 955 956 957 958 959 960 961 962 963 964 965 966
Code Availability. ChimeraLM, implemented in Python, is open source and available on GitHub (https://github.com/ylab-hi/ChimeraLM) under the Apache License, Version 2.0. The package can be installed via PyPI (https://pypi.org/project/chimeralm) using pip, with wheel distributions provided for Windows, Linux, and macOS to ensure easy cross-platform installation. An interactive demo is available on Hugging Face (https://huggingface.co/spaces/yangliz5/ChimeraLM), allowing users to test DeepChopper's functionality without local installation. For large-scale analyses, we recommend using ChimeraLM on systems with GPU acceleration. Detailed system requirements and optimization guidelines are available in the repository's documentation (https://ylab-hi.github.io/ChimeraLM/).	928 929 930 931 932 933 934 935 936 937 938 939 940 941 942 943 944 945 946 947 948 949 950 951 952 953 954 955 956 957 958 959 960 961 962 963 964 965 966
Conflict of interest. RY has served as an advisor/consultant for Tempus AI, Inc. This relationship is unrelated to and did not influence the research presented in this study.	939 940 941 942 943 944 945 946 947 948 949 950 951 952 953 954 955 956 957 958 959 960 961 962 963 964 965 966
Acronyms	943 944 945 946 947 948 949 950 951 952 953 954 955 956 957 958 959 960 961 962 963 964 965 966
CPU Central Processing Unit 12	945
DEL deletion 7, 8	946
DUP duplication 7, 8	948
GLM Genomic Language Model 2, 12	949
GPU Graphics Processing Unit 12, 17, 19, 21	950
HPC High Performance Computing 19	952
INS insertion 7, 8	954
INV inversion 1, 2, 7–9	955
LIANTI Linear Amplification via Transposon Insertion 12	957
MALBAC Multiple Annealing and Looping-based Amplification Cycles 12	959
MDA Multiple Displacement Amplification 2	960
MLP multilayer perceptron 3, 4, 16	961
ONT Oxford Nanopore Technologies 2, 4, 7, 8, 13, 14	962
PacBio Pacific Biosciences 4	963
PTA Primary Template-directed Amplification 12	964
	965
	966

967 **SA** Supplementary Alignment 14, 18, 19
968 **SV** Structural Variation 1–3, 5, 7–13, 15, 18, 19

969
970 **TRA** translocation 2, 7, 8

971
972 **WGA** Whole Genome Amplification 1–8, 10–16, 18–20

973
974 **References**

- 975
976 [1] Kaley-Ezra, E. *et al.* Single-cell somatic copy number variants in brain using
977 different amplification methods and reference genomes. *Communications Biology*
978 1288 (2024).
- 979 [2] Navin, N. *et al.* Tumour evolution inferred by single-cell sequencing. *Nature* **472**,
980 90–94 (2011).
- 982 [3] Sun, C. *et al.* Mapping recurrent mosaic copy number variation in human neurons.
983 *Nature Communications* 4220 (2024).
- 985 [4] Gawad, C., Koh, W. & Quake, S. R. Single-cell genome sequencing: current state
986 of the science. *Nature Reviews Genetics* 175–188 (2016).
- 988 [5] Chen, C. *et al.* Single-cell whole-genome analyses by linear amplification via
989 transposon insertion (LIANTI). *Science (new York, N.Y.)* **356**, 189–194 (2017).
- 991 [6] Macaulay, I. C. & Voet, T. Single cell genomics: Advances and future perspectives.
992 *PLOS Genetics* **10**, e1004126 (2014).
- 993 [7] de Bourcy, C. F. A. *et al.* A quantitative comparison of single-cell whole genome
994 amplification methods. *PLoS ONE* e105585 (2014).
- 996 [8] Biezuner, T. *et al.* Comparison of seven single cell whole genome amplification
997 commercial kits using targeted sequencing. *Scientific Reports* 17171 (2021).
- 999 [9] Lu, N., Qiao, Y., Lu, Z. & Tu, J. Chimera: The spoiler in multiple displacement
1000 amplification. *Computational and Structural Biotechnology Journal* 1688–1696
1001 (2023).
- 1003 [10] Lasken, R. S. & Stockwell, T. B. Mechanism of chimera formation during the
1004 multiple displacement amplification reaction. *BMC Biotechnology* **7**, 19 (2007).
- 1005
- 1006 [11] Agyabeng-Daddie, F. *et al.* Evaluating the benefits and limits of multiple displace-
1007 ment amplification with whole-genome oxford nanopore sequencing. *Molecular*
1008 *Ecology Resources* e14094 (2025).
- 1009
- 1010 [12] Dean, F. B. *et al.* Comprehensive human genome amplification using multiple
1011 displacement amplification. *Proceedings of the National Academy of Sciences* **99**,
1012 5261–5266 (2002).

- [13] Lu, N. *et al.* Exploration of whole genome amplification generated chimeric sequences in long-read sequencing data. *Briefings in Bioinformatics* **24**, bbad275 (2023). 1013
1014
1015
1016
1017
1018
1019
1020
1021
1022
1023
1024
1025
1026
1027
- [14] Sedlazeck, F. J. *et al.* Accurate detection of complex structural variations using single-molecule sequencing. *Nature Methods* 461–468 (2018). 1019
1020
1021
1022
1023
1024
1025
1026
1027
- [15] Smolka, M. *et al.* Detection of mosaic and population-level structural variants with sniffles2. *Nature Biotechnology* 1571–1580 (2024). 1028
1029
1030
1031
1032
1033
1034
1035
1036
1037
1038
1039
- [16] Chen, Y. *et al.* Deciphering the exact breakpoints of structural variations using long sequencing reads with DeBreak. *Nature Communications* 283 (2023). 1028
1029
1030
1031
1032
1033
1034
1035
1036
1037
1038
1039
- [17] Heller, D. & Vingron, M. SVIM: Structural variant identification using mapped long reads. *Bioinformatics* 2907–2915 (2019). 1040
1041
1042
1043
1044
1045
1046
1047
- [18] Jiang, T. *et al.* Long-read-based human genomic structural variation detection with cuteSV. *Genome Biology* 189 (2020). 1048
1049
1050
1051
1052
1053
1054
1055
1056
1057
1058
- [19] Gonzalez-Pena, V. *et al.* Accurate genomic variant detection in single cells with primary template-directed amplification. *Proceedings of the National Academy of Sciences* **118**, e2024176118 (2021). 1048
1049
1050
1051
1052
1053
1054
1055
1056
1057
1058
- [20] Alkan, C., Coe, B. P. & Eichler, E. E. Genome structural variation discovery and genotyping. *Nature Reviews Genetics* **12**, 363–376 (2011). 1048
1049
1050
1051
1052
1053
1054
1055
1056
1057
1058
- [21] Kosugi, S. *et al.* Comprehensive evaluation of structural variation detection algorithms for whole genome sequencing. *Genome Biology* **20**, 117 (2019). 1048
1049
1050
1051
1052
1053
1054
1055
1056
1057
1058
- [22] Kiguchi, Y., Nishijima, S., Kumar, N., Hattori, M. & Suda, W. Long-read metagenomics of multiple displacement amplified DNA of low-biomass human gut phageomes by SACRA pre-processing chimeric reads. *DNA Research* **28**, dsab019 (2021). 1048
1049
1050
1051
1052
1053
1054
1055
1056
1057
1058
- [23] Nguyen, E. *et al.* *HyenaDNA: Long-range genomic sequence modeling at single nucleotide resolution*, Vol. 36, 43177–43201 (Curran Associates, Inc., 2023). 1048
1049
1050
1051
1052
1053
1054
1055
1056
1057
1058
- [24] Dalla-Torre, H. *et al.* Nucleotide transformer: building and evaluating robust foundation models for human genomics. *Nature Methods* 287–297 (2025). 1048
1049
1050
1051
1052
1053
1054
1055
1056
1057
1058
- [25] Zhou, Z. *et al.* *DNABERT-2: Efficient foundation model and benchmark for multi-species genomes*, 1–24 (OpenReview.net, 2024). 1048
1049
1050
1051
1052
1053
1054
1055
1056
1057
1058
- [26] Consens, M. E. *et al.* To transformers and beyond: Large language models for the genome (2023). [arXiv:2311.07621](https://arxiv.org/abs/2311.07621). 1048
1049
1050
1051
1052
1053
1054
1055
1056
1057
1058
- [27] Li, Y. *et al.* A genomic language model for chimera artifact detection in nanopore direct rna sequencing. *bioRxiv* (2024). URL <https://www.biorxiv.org/content/> 1048
1049
1050
1051
1052
1053
1054
1055
1056
1057
1058

- 1059 [early/2024/10/25/2024.10.23.619929](https://doi.org/10.23.619929).
- 1060
- 1061 [28] Routhier, E. & Mozziconacci, J. Genomics enters the deep learning era. *PeerJ*
1062 **10**, e13613 (2022).
- 1063
- 1064 [29] Poli, M. *et al.* *Hyena hierarchy: Towards larger convolutional language models*,
1065 Vol. 202, 28043–28078 (PMLR, 2023).
- 1066
- 1067 [30] Mahmoud, M. *et al.* Structural variant calling: The long and the short of it.
1068 *Genome Biology* **20**, 246 (2019).
- 1069
- 1070 [31] PLC., O. N. Dorado. <https://github.com/nanoporetech/dorado> (2023).
- 1071
- 1072 [32] Martin, M. Cutadapt removes adapter sequences from high-throughput sequenc-
1073 ing reads. *Embnnet.journal* **17**, 10–12 (2011).
- 1074
- 1075 [33] Li, H. Minimap2: Pairwise alignment for nucleotide sequences. *Bioinformatics*
1076 3094–3100 (2018).
- 1077
- 1078 [34] Danecek, P. *et al.* Twelve years of SAMtools and BCFtools. *GigaScience* giab008
1079 (2021).
- 1080
- 1081 [35] De Coster, W. & Rademakers, R. NanoPack2: Population-scale evaluation of
1082 long-read sequencing data. *Bioinformatics* **39**, btad311 (2023).
- 1083
- 1084 [36] Paszke, A. *et al.* *PyTorch: An imperative style, high-performance deep learning*
1085 library, Vol. 32, 8024–8035 (Curran Associates, Inc., 2019).
- 1086
- 1087 [37] Falcon, W. & The PyTorch Lightning team. PyTorch Lightning. GitHub
1088 repository (2019). URL <https://github.com/Lightning-AI/lightning>.
- 1089
- 1090 [38] Loshchilov, I. & Hutter, F. *Decoupled weight decay regularization* (2019).
- 1091
- 1092 [39] Yadan, O. Hydra - a framework for elegantly configuring complex applications.
1093 GitHub repository (2019). URL <https://github.com/facebookresearch/hydra>.
- 1094
- 1095 [40] Chen, X. *et al.* Manta: Rapid detection of structural variants and indels for
1096 germline and cancer sequencing applications. *Bioinformatics* 1220–1222 (2016).
- 1097
- 1098 [41] Rausch, T. *et al.* DELLY: Structural variant discovery by integrated paired-end
1099 and split-read analysis. *Bioinformatics* i333–i339 (2012).
- 1100
- 1101 [42] Wala, J. A. *et al.* SvABA: Genome-wide detection of structural variants and
1102 indels by local assembly. *Genome Research* 581–591 (2018).
- 1103
- 1104 [43] Guo, Q., Li, Y., Wang, T.-Y., Ramakrishnan, A. & Yang, R. OctopusV and
1105 TentacleSV: A one-stop toolkit for multi-sample, cross-platform structural variant
1106 comparison and analysis. *Bioinformatics* btaf599 (2025).

- [44] English, A. C., Menon, V. K., Gibbs, R. A., Metcalf, G. A. & Sedlazeck, F. J. Truvari: Refined structural variant comparison preserves allelic diversity. *Genome Biology* **23**, 271 (2022). 1105
1106
1107
1108
1109
1110
1111
1112
1113
1114
1115
1116
1117
1118
1119
1120
1121
1122
1123
1124
1125
1126
1127
1128
1129
1130
1131
1132
1133
1134
1135
1136
1137
1138
1139
1140
1141
1142
1143
1144
1145
1146
1147
1148
1149
1150